GDCh

Research Article

Angewandte
Chemie
International Edition
www.angewandte.org

Interfaces

Controllable Graphene/MoS$_2$ Heterointerfaces by Perpendicular Surface Functionalization

Qing Cao$^+$, Jiajun Dai$^+$, Zhuting Hao, Beate Paulus, Siegfried Eigler, and Xin Chen*

Abstract: Surface chemistry and interface interactions profoundly influence the properties of two-dimensional (2D) materials and heterostructures. Therefore, developing methods to precisely control surfaces and interfaces is crucial for harnessing the properties and functions of 2D materials and heterostructures. Here, we developed a facile approach to tuning the interface distance and properties of graphene/MoS$_2$ heterostructures (G/MoS$_2$) by varying the functional groups attached to the surface of graphene bottom layer. We systematically investigated how different functionalized graphene bottom layers affect the interlayer distance, coupling between the interlayers, and optical properties of resulting G/MoS$_2$ heterostructures. Our findings indicate that both the size and electron-withdrawing/donating properties of functional groups are pivotal in regulating charge transport properties, with size playing a particularly decisive role. Our approach demonstrates an efficient and flexible pathway to regulate the interlayer spacing and charge transport, highlighting the potential of engineering interface chemistry in optimizing properties of van der Waals heterostructures.

Introduction

Since the first exfoliation of graphene,[1] the family of two-dimensional (2D) materials has made impressive developments.[2] These 2D materials exhibit exceptional characteristics in optics, electronics, mechanics, and magnetics, differentiating them from their bulk counterparts.[3] The combination of different types of 2D materials into vertical stacks, known as van der Waals (vdW) heterostructures, enables the synergetic effects of different components and overcomes the limitations of individual materials, opening up a new realm of possibilities.[4] Among the heterostructures investigated so far, graphene/MoS$_2$ heterostructures (G/MoS$_2$) integrating the superior charge mobility of graphene with the direct band gap semiconductor MoS$_2$, are particularly notable for their potential in high performance electronic and optoelectronic devices.[5] The interfacial interactions between graphene and MoS$_2$ layers are found to determine their physical properties and device performance.[5-6] For example, derivatives of graphene, such as graphene oxides and defect-rich porous graphene, stacked with MoS$_2$ have been fabricated to modulate the charge redistribution, thereby inducing a p-doping effect in MoS$_2$.[7] Especially, the interlayer distance strongly influences charge transfer, which plays a significant role in shaping the electronic and optical behaviors of the heterostructures.[8]

However, once the vdW interface is formed, tuning the vdW interactions, especially the interface distance of heterostructures at the nanoscale, is not a trivial task. This is because the material layers tend to maintain the lowest energy level of the interactions—i.e., the most stable arrangement—unless external perturbations, such as intercalation techniques,[9] are applied. In our recent report, we showcased a straightforward strategy to modulate the interfacial interactions of G/MoS$_2$ heterostructures by pre-functionalizing graphene with oligophenyl groups and subsequently assembling the vdW structures.[10] An interlayer distance of 8 nm was achieved in functionalized G/MoS$_2$ heterostructures (F-G/MoS$_2$) due to the oligophenyl groups on graphene serving as spacers. This configuration led to a 5-fold increase in the photoluminescence (PL) intensity of MoS$_2$, compared to a 1.8-fold enhancement with the reversed stacking order, demonstrating the potential of using functional groups to tailor interface coupling and optical properties of heterostructures.[10] It is noted that diazonium chemistry-assisted pre-functionalization of graphene lacks control over the size and thickness of functional groups, leading to insufficient control of interlayer distances. Additionally, this method is limited to introducing aromatic spacers. Thus, a universal approach for precisely tuning heterointerfaces towards an improved function is highly desirable.

Here we present a chemical strategy for systematically and efficiently tuning the heterointerfaces of G/MoS$_2$ heterostructures. Four types of functionalized graphene, each perpendicularly tethered with a distinct type of functional group (methyl: CH$_3$-; tert-butyl: C$_4$H$_9$-; trifluorometh-

[*] Dr. Q. Cao,$^+$ Z. Hao, Prof. Dr. S. Eigler, Dr. X. Chen
Institute of Chemistry and Biochemistry
Freie Universität Berlin
Altensteinstraße 23a, 14195 Berlin, Germany
E-mail: xin.chen@fu-berlin.de

J. Dai,$^+$ Prof. Dr. B. Paulus
Institute of Chemistry and Biochemistry
Freie Universität Berlin
Arnimallee 22, 14195 Berlin, Germany

[$^+$] These authors contribute equally to this work.

yl: CF$_3$-; pentafluoroethyl: C$_2$F$_5$-) that varies in size and electron-withdrawing/donating properties, are used as the bottom layer. These functionalized graphene layers were prepared by reacting graphene with hypervalent iodine compounds in a mild and controllable way. Monolayers of MoS$_2$ serve as the top layer, creating distinct heterointerfaces. By varying the length of the functional group, we can precisely tune the interlayer distance on the nanometer scale. The interlayer charge transfer, interlayer distance, and binding energy of the different functionalized G/MoS$_2$ heterostructures are investigated in detail using Raman and PL spectroscopies and density functional theory (DFT) calculations. Critically, we disentangled the structure–property relationship between the molecular spacer and the charge transfer of the assembled G/MoS$_2$ heterostructures, which offers a practical foundation for systematically tailoring the heterostructures and their optical and electronic properties.

Results and Discussion

The fabrication process of functionalized G/MoS$_2$ heterostructures is shown in Scheme 1, which starts with the laser-induced functionalization of graphene with hypervalent iodine compounds followed by the stacking of mechanically exfoliated monolayer MoS$_2$ on top (Scheme 1). Hypervalent iodine compounds were chosen as the photoreactive reagents due to their ease of handling and high efficiency in generating reactive radical intermediates upon photon irradiation. These intermediates can react with graphene,

resulting in a high degree of functionalization with diverse functional groups and minimal side reactions.[11] The chemical vapor deposition (CVD) graphene film was firstly transferred on a Si/SiO$_2$ substrate marked with gold alignment markers (Scheme 1a) for subsequent location of specific regions (Figure S1). The graphene sample was then drop-coated with a thin layer of photoreactive reagent, including pre-dissolved hypervalent iodine compounds such as (diacetoxyiodo)benzene, [bis(trifluoroacetoxy)iodo]benzene, acid pentafluoroethyl-Togni reagent, and bis(*tert*-butylcarbonyloxy)iodobenzene (Scheme 1b). Subsequently, a 532 nm Raman laser was directly focused onto the sample surfaces to trigger the decomposition of the hypervalent iodine compounds (Scheme 1c), upon which reactive CH$_3$•, CF$_3$•, C$_2$F$_5$•, and C$_4$H$_9$• radicals were generated, exclusively at the irradiated regions. These generated radicals immediately reacted with the underlying graphene, resulting in the covalently functionalized graphene domains (Scheme 1f). Afterward, the unreacted reagents and physisorbed by-products were washed away by rinsing with acetone, leaving behind only the functionalized graphene domains with CH$_3$-, CF$_3$-, C$_2$F$_5$-, and C$_4$H$_9$- groups covalently bonded on the graphene surface, denoted as CH$_3$-G, CF$_3$-G, C$_2$F$_5$-G, and C$_4$H$_9$-G, respectively (Scheme 1d). In the last step, mechanically exfoliated monolayers of MoS$_2$ were transferred onto the functionalized regions of the graphene films using a stamping technique with gold alignment markers, forming CH$_3$-G/MoS$_2$, CF$_3$-G/MoS$_2$, C$_2$F$_5$-G/MoS$_2$, and C$_4$H$_9$-G/MoS$_2$ heterostructures (Scheme 1e).

To ensure relatively uniform separation of heterostructure layers using functional group-based spacers, a high
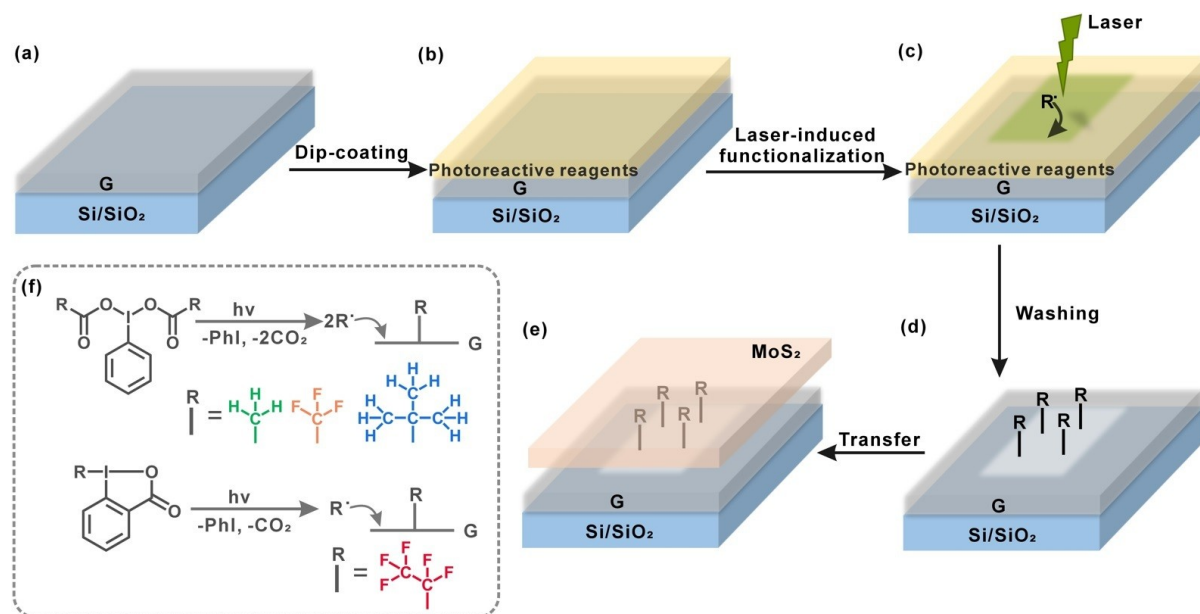
Scheme 1. (a–e) Schematic of the fabrication process for functionalized G/MoS$_2$ heterostructures on a Si/SiO$_2$ substrate. In 1c, the laser-irradiated area is highlighted in green, and in 1d, the white region shows the functionalized graphene domain after washing. (f) Graphic illustration of the formation of functionalized graphene domains *via* laser-triggered covalent addition reactions. This process involves the laser photon-initiated decomposition of hypervalent iodine compounds to generate reactive radicals (R•), followed by the covalent addition of these radicals to the top side of graphene. The local strain induced by covalent functionalization is likely relieved through antaratopic binding of H or OH groups to the bottom side of graphene.

degree of covalent functionalization of graphene in the laser-irradiated regions is desired. To achieve this, we systematically screened various laser irradiation conditions, including both irradiation time (T) and laser power (E) (Figures S2–S5). Taking CH_3-G for example, the Raman spectra recorded at the same irradiation time (1 ms) showed an increased intensity of the D-band at 1350 cm^{-1}, a decreased intensity of the 2D-band at 2680 cm^{-1}, and broadening of the G-band at 1582 cm^{-1} as the laser power was increased (E = 1.71, 2.02, 2.34, and 2.66 mW). A similar trend was observed when the sample was exposed to the same laser power but with extended irradiation time. This suggests that the graphene lattice becomes increasingly functionalized with higher laser power and longer irradiation time. These defects were likely introduced by the addition of methyl radicals to the top side of the graphene and through interactions with the silicon substrate on the bottom side, which relieved the built-up strain. Therefore, a higher degree of graphene functionalization can be achieved by simply applying higher laser power and extended irradiation time. We also noted the presence of impurities in some irradiated regions (Figures S2c and S5c), which appeared only when higher laser power or longer irradiation times were applied. These impurities likely arise from unreacted reagent residues or byproducts, such as dimers of radicals, physisorbed on the graphene surface. Given that these impurities can affect the quality and interlayer properties of the assembled heterostructures, we identified specific parameters for each functionalized sample to achieve a highly functionalized and clean graphene surface: CH_3-G (E = 2.02 mW, T = 1 ms), CF_3-G (E = 1.80 mW, T = 5 ms), C_2F_5-G (E = 3.53 mW, T = 0.5 ms), and C_4H_9-G (E = 3.30 mW, T = 1 ms). The microscopic images of CH_3-G, CF_3-G, C_2F_5-G, and C_4H_9-G are displayed in Figure S6. The functionalized areas of graphene display no obvious differences compared to the non-functionalized areas of graphene in the optical images.

The average Raman spectra and the corresponding statistical histograms of the Raman intensity ratio (I_D/I_G), defined as the integrated peak area ratio of the D- and G-bands, for pristine graphene and functionalized CH_3-G, CF_3-G, C_2F_5-G, and C_4H_9-G are depicted in Figures 1a and 1b. The parameters, including peak area and full width at half maximum (FWHM) for the fitted D-, G-, and 2D- bands in Figure 1a, obtained using the Lorentzian function, are summarized in Table S1. Compared to pristine graphene, the Raman spectra of irradiated parts of CH_3-G, CF_3-G, C_2F_5-G, and C_4H_9-G show an intense D-band, attenuated 2D-band and broadening of G-band (with the appearance of a D'-band at 1620 cm^{-1}), confirming the successful functionalization of graphene. The average values of I_D/I_G for CH_3-G, CF_3-G, C_2F_5-G, and C_4H_9-G are 1.46, 2.18, 1.43, and 2.71, corresponding to degrees of functionalization (θ) of 2.44 %, 1.06 %, 2.55 %, and 0.64 %, respectively, based on the I_D/I_G-θ model (Figures S2–S5).[12] The high degree of functionalization is likely due to the highly efficient antaratopic addition process, where the top side is functionalized with functional groups, while the bottom side—facing the SiO_2 layer, which contains Si-OH groups and adsorbed water—

undergoes addition with groups such as hydroxyl (-OH).[13] The lowest degree of functionalization observed in C_4H_9-G is likely due to the steric hindrance caused by the *tert*-butyl group, which impeded the addition of functional groups to adjacent atoms.

Raman spectra (Figure 1c) of all the functionalized G/MoS_2 heterostructures consist of characteristic features of both monolayer MoS_2 and graphene. Two Raman peaks of MoS_2, the in-plane breathing mode (E^1_{2g}, 385.4 cm^{-1}) and the out-of-plane vibration mode (A_{1g}, 404.1 cm^{-1}), were clearly detected. The magnified Raman spectra of MoS_2 in the range of 340–460 cm^{-1} are shown in Figure 1d. In pristine MoS_2, the frequency difference between E^1_{2g} and A_{1g} is 18.7 cm^{-1}, confirming its monolayer characteristic.[14] The E^1_{2g} mode is sensitive to lattice distortions or strain in MoS_2.[14c] The frequency of E^1_{2g} modes of all the heterostructures slightly shifted (by 0.7 cm^{-1}) to lower frequencies compared to that of pristine MoS_2, indicating that a small degree of strain was introduced in MoS_2 by stacking it with either pristine or functionalized graphene.[15] The A_{1g} mode is sensitive to charge-doping.[5,16] Compared to the A_{1g} mode of pristine MoS_2, the A_{1g} mode of G/MoS_2, CH_3-G/MoS_2 and C_4H_9-G/MoS_2 heterostructures shifts to a higher frequency by about 1.3 cm^{-1}, indicating n-doping of MoS_2. In contrast, there are slight downshifts of the A_{1g} mode by about 0.5 cm^{-1} in the CF_3-G/MoS_2 and C_2F_5-G/MoS_2 heterostructures, indicating a p-doping effect likely caused by the CF_3- and C_2F_5-functional groups.

The microscope images of corresponding CH_3-G/MoS_2, CF_3-G/MoS_2, C_2F_5-G/MoS_2, and C_4H_9-G/MoS_2 heterostructures are shown in Figures 2a–d. Atomic force microscopy (AFM) images of CH_3-G/MoS_2, CF_3-G/MoS_2, C_2F_5-G/MoS_2, and C_4H_9-G/MoS_2 heterostructures are shown in Figure S7. The height profiles were measured across unfunctionalized regions to functionalized regions on the heterostructures. An increase in thickness was observed: 1 nm for CH_3-G/MoS_2 and CF_3-G/MoS_2, 1.5 nm for C_2F_5-G/MoS_2, and 2 nm for C_4H_9-G/MoS_2. This increase reflects the expanded interlayer distance, likely resulting from the introduction of functional groups in the interlayer space. To account for the potential surface irregularities and local variations, we measured the statistical height distribution within both G/MoS_2 and functionalized G/MoS_2 regions (Figure S8). The values and trends in height increases closely align with the step heights shown in Figure S7. Importantly, the general trend in measured interlayer distances correlates well with the size of the functional groups, suggesting that our control over the interlayer distance is consistent and reliable.

The impact of forming functionalized G/MoS_2 interfaces on the optical properties of MoS_2 was characterized using Raman and PL spatial mapping. As the functionalized graphene resulted in an increased peak intensity ratio of D-band to G-band, the functionalized regions of graphene can be clearly identified as the regions with higher I_D/I_G values in the corresponding Raman maps (Figures 2e–h). The differences in intensity ratios within the irradiated region suggest that the degree of functionalization varies, likely due to local variations in reagent concentration. PL intensity maps of functionalized G/MoS_2 heterostructures recorded
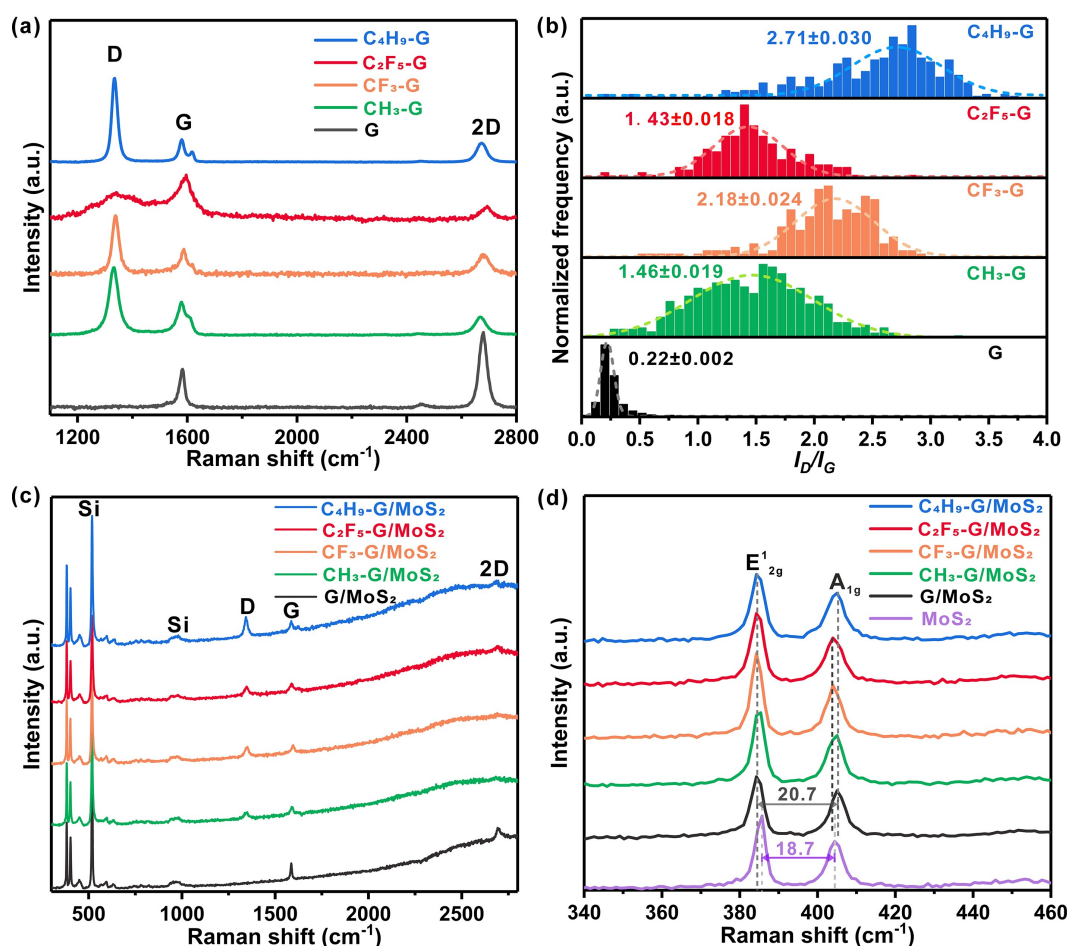
Figure 1. (a) Raman spectra ($\lambda_{ex} = 532$ nm) and (b) statistical Raman I_D/I_G histograms for pristine graphene (G), CH_3-G, CF_3-G, C_2F_5-G, and C_4H_9-G. The I_D/I_G values in the statistical Raman histograms for functionalized graphene samples are based on peak area ratios obtained from Lorentzian fitting. The Raman spectrum of C_2F_5-G shows a significantly broader D-band compared to other functionalized graphene samples, likely due to its high degree of functionalization (2.55%). (c) Raman spectra of G/MoS_2, CH_3-G/MoS_2, CF_3-G/MoS_2, C_2F_5-G/MoS_2, and C_4H_9-G/MoS_2 heterostructures. (d) Enlarged Raman spectra of pristine MoS_2, G/MoS_2, CH_3-G/MoS_2, CF_3-G/MoS_2, C_2F_5-G/MoS_2, and C_4H_9-G/MoS_2 heterostructures. All Raman spectra are plotted with a Y-axis offset for clarity. The dashed lines in (d) indicate the positions of the E^1_{2g} and A_{1g} modes of MoS_2.

under the same irradiation conditions are depicted in Figures 2i–l. The regions, which consist of both functionalized graphene (black dashed block) and monolayer MoS_2 (red dashed block), show enhanced PL intensity of MoS_2 compared to regions containing non-functionalized G and MoS_2, indicating that the radiative recombination efficiency of MoS_2 was significantly improved when using functionalized graphene as the support layer. The inhomogeneous distribution of PL intensity in the heterostructure region was observed, presumably caused by the spatial variation of the functionalized graphene support layer (Figures 2e–h). Despite of this, the largest area of uniform PL enhancement, approximately 5×5 μm^2, was achieved with C_4H_9-G/MoS_2 (Figure 2l).

To gain more insights into the PL behavior of functionalized G/MoS_2 heterostructures, a detailed analysis of average PL spectra of all investigated heterostructures was performed (Figures 3 and S9). The PL of G/MoS_2 is quenched by 2 times compared to pristine MoS_2, due to the

strong electronic interactions and charge transfer from graphene to MoS_2. The PL intensity maxima of functionalized G/MoS_2 heterostructures are all enhanced compared to pristine G/MoS_2: 2.6 times for CH_3-G/MoS_2, 3.5 times for CF_3-G/MoS_2, 4.5 times for C_2F_5-G/MoS_2, and 5.0 times for C_4H_9-G/MoS_2. This is in good agreement with the PL mapping experiments shown in Figures 2i–l.

Lorentzian deconvolution of PL spectra of pristine G/MoS_2 and functionalized G/MoS_2 revealed three peaks corresponding to the neutral exciton (A^0, 1.89 eV), negatively charged trion (A^-, 1.85 eV), and B exciton (2.02 eV) (Figure S9, Table S2). The A^0 exciton results from transitions between the lower spin-orbit split valence band and the conduction band minimum, while the B exciton involves the higher spin-orbit split valence band.[17] The A^- trion consists of an A^0 exciton bound with an additional electron. Therefore, the relative concentration of charged excitons to neutral excitons (A^-/A^0), estimated by the spectra weight of the corresponding peak, can reflect the doping level in
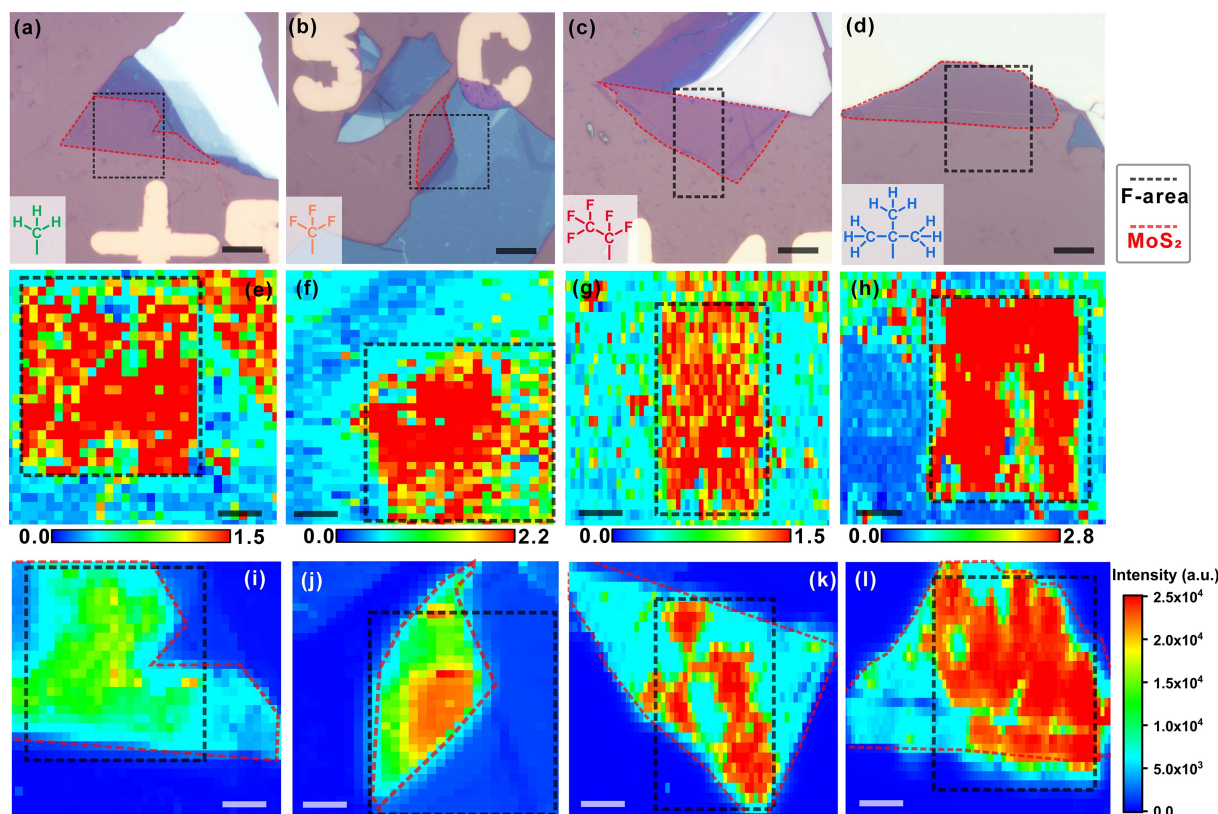
Figure 2. (a–d) Optical microscope images, (e–h) corresponding Raman ($\lambda_{ex} = 532$ nm) I_D/I_G maps, and (i–l) PL intensity maps of MoS$_2$ in CH$_3$-G/ MoS$_2$, CF$_3$-G/MoS$_2$, C$_2$F$_5$-G/MoS$_2$, and C$_4$H$_9$-G/MoS$_2$ heterostructures, respectively. For comparison of PL enhancement, Figures (i–l) use the same intensity scale shown on the right. (Scale bar: 5 μm in a–d; 2 μm in e–l.) Functionalized graphene areas and monolayer MoS$_2$ are outlined by black and red dashed blocks, respectively.
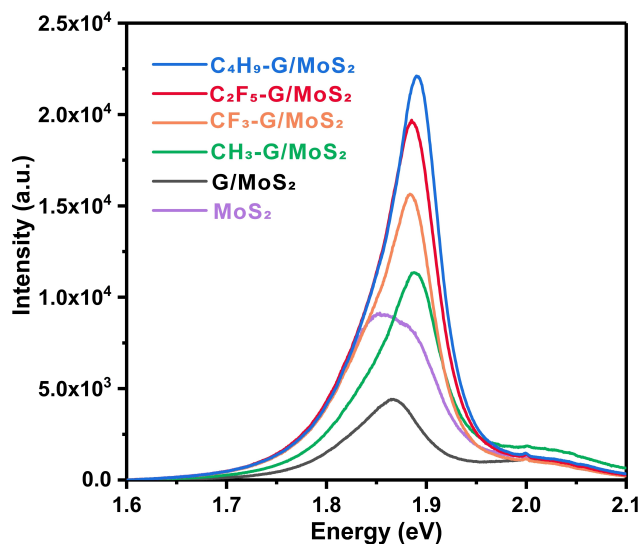
Figure 3. Comparison of PL ($\lambda_{ex} = 532$ nm) spectra of pristine MoS$_2$, G/ MoS$_2$, CH$_3$-G/MoS$_2$, CF$_3$-G/MoS$_2$, C$_2$F$_5$-G/MoS$_2$, and C$_4$H$_9$-G/MoS$_2$ heterostructures. The peak at 2.0 eV, corresponding to the 2D-band of graphene, becomes weakened in the PL spectra of functionalized G/ MoS$_2$ heterostructures due to the functionalization of graphene.

MoS$_2$. The PL spectrum of pristine MoS$_2$ is dominated by the trion peak, signifying the n-type doping of MoS$_2$ (Figure S9). The PL spectrum of G/MoS$_2$ exhibits a stronger contribution from the A$^-$ peak, indicating electron transfer from graphene into MoS$_2$. This increased charge carrier concentration can lead to enhanced non-radiative recombination, resulting in a reduced PL intensity as shown in Figure 3. In comparison, the PL spectra of functionalized G/ MoS$_2$ heterostructures (Figure S9) are dominated by the A^0 neutral exciton, suggesting that the n-doping effect has been significantly diminished. Additionally, the increased contribution of neutral excitons in the functionalized G/MoS$_2$ heterostructures causes a blue shift in the PL spectrum (Figure 3). A close inspection of fitted PL spectra and relative population of A^0 revealed that the peak intensity of A^0 exciton of CH$_3$-G/MoS$_2$, CF$_3$-G/MoS$_2$, C$_2$F$_5$-G/MoS$_2$, and C$_4$H$_9$-G/MoS$_2$ are 6.6, 8.7, 11.4, 13.3 times higher than that of G/MoS$_2$, respectively. It is expected that employing a strong p-doped graphene layer such as CF$_3$-G and C$_2$F$_5$-G can promote electron transfer from MoS$_2$ to the functionalized graphene, enhancing the formation of neutral excitons by combining extra holes with electrons.

To recap, we have thoroughly characterized both pristine G/MoS$_2$ and functionalized G/MoS$_2$ heterostructures using AFM, Raman, and PL spectroscopy. The interlayer distance increases in the following order: G/MoS$_2$, CH$_3$-G/MoS$_2$, CF$_3$-

G/MoS_2, C_2F_5-G/MoS_2, C_4H_9-G/MoS_2. Unlike pristine graphene, which quenches the PL of MoS_2, employing functionalized graphene as the bottom layer results in a pronounced enhancement of the PL signal in MoS_2. The PL intensity of heterostructures increases in the following order: G/MoS_2, CH_3-G/MoS_2, CF_3-G/MoS_2, C_2F_5-G/MoS_2, C_4H_9-G/MoS_2. Interestingly, the degree of PL enhancement positively correlates with the interlayer distance, regardless of the type of functionalized graphene.

DFT Study

To gain a better understanding of the different heterointerfaces and their effects on the PL behavior of the top layer MoS_2, we modeled the structures of both pristine G/MoS_2 and functionalized G/MoS_2 heterostructures and calculated the interlayer charge transfer, interlayer distance, and vdW interaction using DFT at the Perdew–Burke–Ernzerhof (PBE) level[18] with the Tkatchenko–Scheffler (TS) dispersion correction[19] method. As shown in Figure 4a, the pristine G/MoS_2 heterostructure was calculated in a 5:4 supercell setting and the interlayer distance between graphene and MoS_2 is 3.39 Å, which is in good agreement with a previous report of 3.40 Å.[20] The Bader charge difference analysis (Figure 4f) showed that graphene transferred 0.041 e to MoS_2 in total, which corroborates well with the n-doping effect observed in our Raman measurements (Figure 1d). For the functionalized G/MoS_2 systems, the same 5:4 supercell settings were used. To simulate the experimental degree of functionalization between 0.64 % and 2.55 %, we used one functional group per 50 carbon atoms of graphene, resulting in a 2 % coverage. The equalized surface coverage in DFT excludes the influence of dopant concentration, facilitating the comparison of charge transfer ability in the idealized systems. The optimized structure of CH_3-G/MoS_2, C_4H_9-G/MoS_2, CF_3-G/MoS_2, and

C_2F_5-G/MoS_2 are displayed in Figures 4b–e. The calculated interlayer equilibrium distances are 3.87 Å, 4.94 Å, 5.95 Å and 6.64 Å for CH_3-G/MoS_2, CF_3-G/MoS_2, C_4H_9-G/MoS_2, and C_2F_5-G/MoS_2, respectively. The trend in interlayer distance aligns reasonably well with our AFM measurements but significantly smaller in magnitude (Figure S7). The discrepancies between the calculated interlayer equilibrium distances and the AFM-measured interlayer distances can be attributed to the fact that the calculated values reflect the intrinsic equilibrium under ideal conditions, while the AFM measurements capture real-world factors such as surface roughness, degree of functionalization, strain, stacking configuration, and wrinkles or bubbles formed during sample preparation.[21] The binding energies of heterolayers were found to be −5.14 eV, −3.37 eV, −2.47 eV, −2.50 eV, and −1.93 eV (per supercell) for G/MoS_2, CH_3-G/MoS_2, CF_3-G/MoS_2, C_4H_9-G/MoS_2, and C_2F_5-G/MoS_2, respectively. Compared to G/MoS_2, the interaction between layers in the functionalized G/MoS_2 is weakened considerably due to the increased interlayer distance. The C_2F_5-G/MoS_2 heterostructure exhibits the weakest binding energy among all the heterostructures due to the largest interlayer distance. The large interlayer distances and low binding energies at the functionalized graphene/MoS_2 interfaces indicate very weak interactions. Therefore, the MoS_2 monolayer is nearly freestanding in the functionalized G/MoS_2 samples.

The electric dipole formed due to charge transfer has a significant influence on the electronic structure of MoS_2. We first performed the Bader charge difference calculation to evaluate the influence of interlayer difference and functional groups on the electronic structure of MoS_2. It's worth noting that the charge redistribution doesn't just take place within the material. Electron transfer between the functional groups and MoS_2 can also be observed. Therefore, doping of MoS_2 results from the charge transfer from both the graphene basal plane and the functional groups. As depicted in Figures 4f–j, electron injection into MoS_2 (n-doping) was
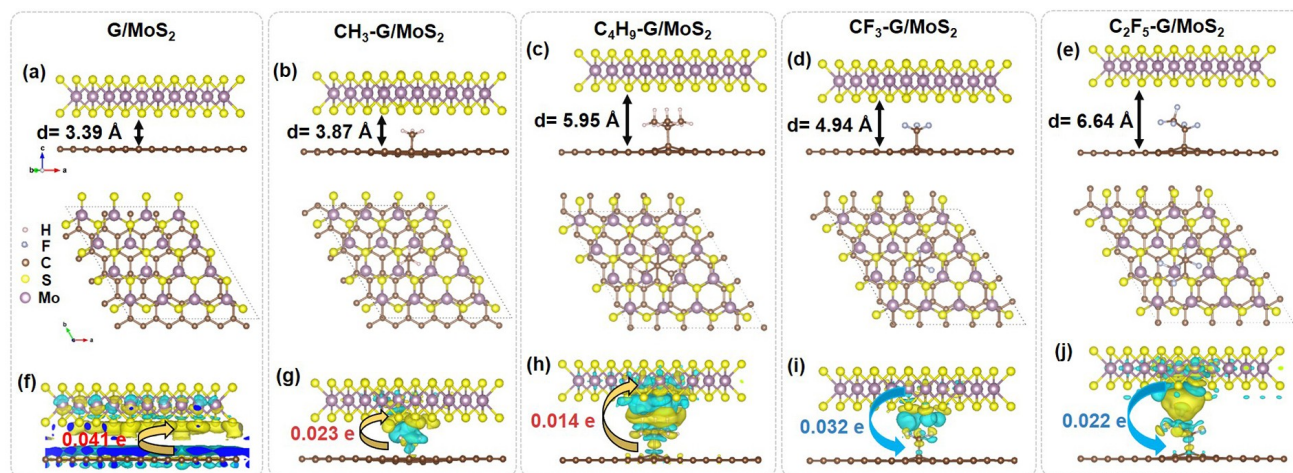
Figure 4. (a–e) Optimized structures obtained with PBE + TS of G/MoS_2, CH_3-G/MoS_2, C_4H_9-G/MoS_2, CF_3-G/MoS_2, and C_2F_5-G/MoS_2. The interlayer distance is represented by *d*. (f–j) Bader charge density difference of G/MoS_2, CH_3-G/MoS_2, C_4H_9-G/MoS_2, CF_3-G/MoS_2, and C_2F_5-G/MoS_2. The yellow and blue areas represent electron accumulation and depletion, respectively, with the charge density difference shown at a contour value of 0.00006 e Å^{-3}). The arrow indicates the direction of electron transfer.

observed in G/MoS$_2$, CH$_3$-G/MoS$_2$, and C$_4$H$_9$-G/MoS$_2$, while electron removal from MoS$_2$ (p-doping) was observed in CF$_3$-G/MoS$_2$ and C$_2$F$_5$-G/MoS$_2$. The electron transfers in different heterostructures, calculated by DFT, are consistent with the MoS$_2$ Raman A$_{1g}$ mode shift observations (Figure 1d). In the category where the MoS$_2$ is n-doped, the MoS$_2$ layer in CH$_3$-G/MoS$_2$ is negatively charged with 0.023 e, which is lower than the 0.041 e charge in G/MoS$_2$ (Figure 4f). Furthermore, C$_4$H$_9$-G, which bears the most electron-donating functional groups, transfers only 0.014 e to MoS$_2$, even less than CH$_3$-G/MoS$_2$ (Figure 4g). This implies that the electron-donating functional groups on graphene did not improve the electron transfer ability; instead, they led to a weakened doping effect to the MoS$_2$ top layer (Figure 4h). Such a weakened n-doping effect was observed in the PL spectra of CH$_3$-G/MoS$_2$ and C$_4$H$_9$-G/MoS$_2$, where the concentration of charged trions significantly decreased compared to G/MoS$_2$ (Figure S9 and Table S2). In the category where the MoS$_2$ was p-doped, MoS$_2$ is positively charged with 0.032 and 0.022 e removed in CF$_3$-G/MoS$_2$ and C$_2$F$_5$-G/MoS$_2$, respectively (Figures 4i–j and Figure S10). This also coincides with our experimental results. Specifically, the concentration of neutral excitons surpasses that of charged trions in the PL spectra of CF$_3$-G/MoS$_2$ and C$_2$F$_5$-G/MoS$_2$, likely due to the p-doping of MoS$_2$ (Figure S9 and Table S2). Interestingly, in both n-type and p-type categories, at the same dopant concentration (surface coverage), a higher number of transferred electrons—and thus a higher concentration of charge carriers—was observed not in samples with the most electron-donating or electron-withdrawing groups, but in those with smaller interlayer distances and stronger binding energies. However, in our experiments, samples with smaller interlayer distances, such as CH$_3$-G/MoS$_2$ and CF$_3$-G/MoS$_2$, showed lower PL intensity enhancement despite the strong doping effect. In contrast, samples with larger interlayer distances, such as C$_2$F$_5$-G/MoS$_2$ and C$_4$H$_9$-G/MoS$_2$, exhibited higher PL intensity enhancement. This indicates that charge transfer was not the only factor impacting the PL of MoS$_2$. Other factors, such as strain, interface dopants, and the thermal conductivity of the functionalized graphene, may also affect PL intensity by influencing exciton formation and stability, non-radiative recombination pathways, the Fermi level, and heat dissipation. A more detailed investigation into the origin of PL intensity enhancement is beyond the scope of this work.

Figure S11 shows the element-projected band structure of G/MoS$_2$ without spin-orbit coupling (SOC). The electronic states of different wave vectors have electron orbitals with different spatial distributions. The band structure is a superposition of the expected band structure of graphene, with the Dirac cone at the Fermi level and the semiconduction band structure of MoS$_2$ with a fundamental band gap of 1.78 eV at the PBE level. Furthermore, we calculated the band structure of the functionalized G/MoS$_2$ heterostructures (Figure S12). The band contributed by functionalized graphene indicates an emerging band gap in graphene due to functionalization. The band contributed by MoS$_2$ shows that the MoS$_2$ layer retains its direct band gap at the K point, with a band gap of 1.71–1.72 eV. The negligible change in the band gap indicates that the electronic structure of MoS$_2$ is maintained in the functionalized G/MoS$_2$ heterostructures.[8] A summary of the results, including interlayer distance, binding energy, charge transfer, degree of functionalization, MoS$_2$ band gap, and PL intensity for different functionalized G/MoS$_2$ heterostructures, can be found in Tables S3 and S4.

Conclusion

We have developed a straightforward strategy to create and control G/MoS$_2$ heterointerfaces by pre-functionalizing the graphene bottom layer with various functional groups. By adjusting the backbone size of these functional groups, we can systematically tune the interlayer distance at the nanometer scale. The increased interlayer distance weakens the binding energy of the heterolayers, significantly reducing charge transfer efficiency and leading to a decreased population of charge carriers in MoS$_2$. The modulation of charge transport, in turn, profoundly influences the PL emission of MoS$_2$. Our strategy offers substantial flexibility in tailoring the interlayer spacing and charge transport in 2D heterostructures. This concept can be applied to various vdW interfaces beyond semiconductor/metal interfaces, enhancing the properties and performance of the resulting devices.

Supporting Information

Microscopic image of CVD graphene film (Figure S1). Laser-induced functionalization of graphene under different laser power and irradiation time (Figure S2–S5). Microscopic images of functionalized graphene (Figure S6). AFM images and height profiles of functionalized G/MoS$_2$ (Figure S7 and S8). PL Peak fittings for pristine MoS$_2$, G/MoS$_2$ and functionalized G/MoS$_2$ (Figure S9). Bader charge density difference of p-type functionalized G/MoS$_2$ (Figure S10). Band structure of G/MoS$_2$ (Figure S11) and functionalized G/MoS$_2$ (Figure S12). Parameters about fitted Raman peaks of graphene by the Lorentz function (Table S1). Parameters about fitted PL peaks by the Lorentz function (Table S2). Summary of interfacial variations induced by p-type functional groups (Table S3) and n-type functional groups (Table S4) in G/MoS$_2$.

Acknowledgements

Conflict of Interest

The authors declare no conflict of interest.

Data Availability Statement

The data that support the findings of this study are available from the corresponding author upon reasonable request.

[1] K. S. Novoselov, A. K. Geim, S. V. Morozov, D. Jiang, Y. Zhang, S. V. Dubonos, I. V. Grigorieva, A. A. Firsov, *Science* **2004**, *306*, 666–669.

[2] a) H. Zhang, *ACS Nano* **2015**, *9*, 9451–9469; b) S. Z. Butler, S. M. Hollen, L. Cao, Y. Cui, J. A. Gupta, H. R. Gutierrez, T. F. Heinz, S. S. Hong, J. Huang, A. F. Ismach, E. Johnston-Halpern, M. Kuno, V. V. Plashnitsa, R. D. Robinson, R. S. Ruoff, S. Salahuddin, J. Shan, L. Shi, M. G. Spencer, M. Terrones, W. Windl, J. E. Goldberger, *ACS Nano* **2013**, *7*, 2898–2926; c) R. Mas-Balleste, C. Gomez-Navarro, J. Gomez-Herrero, F. Zamora, *Nanoscale* **2011**, *3*, 20–30.

[3] a) Y. Cao, V. Fatemi, A. Demir, S. Fang, S. L. Tomarken, J. Y. Luo, J. D. Sanchez-Yamagishi, K. Watanabe, T. Taniguchi, E. Kaxiras, R. C. Ashoori, P. Jarillo-Herrero, *Nature* **2018**, *556*, 80–84; b) C. Lee, X. Wei, J. W. Kysar, J. Hone, *Science* **2008**, *321*, 385–388; c) P. Sun, K. Wang, H. Zhu, *Adv. Mater.* **2016**, *28*, 2287–2310; d) G. Fiori, F. Bonaccorso, G. Iannaccone, T. Palacios, D. Neumaier, A. Seabaugh, S. K. Banerjee, L. Colombo, *Nat. Nanotechnol.* **2014**, *9*, 768–779; e) A. Splendiani, L. Sun, Y. Zhang, T. Li, J. Kim, C. Y. Chim, G. Galli, F. Wang, *Nano Lett.* **2010**, *10*, 1271–1275.

[4] a) N. R. Glavin, S. Nam, *Matter* **2023**, *6*, 4–6; b) A. K. Geim, I. V. Grigorieva, *Nature* **2013**, *499*, 419–425; c) X. Chen, M. Assebban, M. Kohring, L. Bao, H. B. Weber, K. C. Knirsch, A. Hirsch, *J. Am. Chem. Soc.* **2022**, *144*, 9645–9650; d) K. S. Novoselov, A. Mishchenko, A. Carvalho, A. H. Castro Neto, *Science* **2016**, *353*, aac9439; e) X. Liu, M. C. Hersam, *Adv. Mater.* **2018**, *30*, 1801586.

[5] M. Yang, L. Wang, G. Hu, X. Chen, P. L. Gong, X. Cong, Y. Liu, Y. Yang, X. Li, X. Zhao, X. Liu, *Nano Res.* **2021**, *14*, 2241–2246.

[6] a) W. Hu, T. Wang, R. Zhang, J. Yang, *J. Mater. Chem. C* **2016**, *4*, 1776–1781; b) J. Zhou, H. Zhao, X. Fan, K. Yuan, Z. Wang, Z. Zhang, D. Li, X. Zhang, H. Chen, D. Tang, X. Zheng, J. Zhu, *Mater. Today Phys.* **2023**, *38*, 101272.

[7] a) Z. Wang, Q. Cao, K. Sotthewes, Y. Hu, H. S. Shin, S. Eigler, *Nanoscale* **2021**, *13*, 15464–15470; b) Y. Wang, C. Neumann, M. Hußmann, Q. Cao, Y. Hu, O. Garrity, P. Kusch, A. Turchanin, S. Eigler, *Adv. Mater. Interfaces* **2021**, *8*, 2100783; c) H. M. Oh, H. Jeong, G. H. Han, H. Kim, J. H. Kim, S. Y. Lee, S. Y. Jeong, S. Jeong, D. J. Park, K. K. Kim, Y. H. Lee, M. S. Jeong, *ACS Nano* **2016**, *10*, 10446–10453.

[8] Q. Fang, M. Li, X. Zhao, L. Yuan, B. Wang, C. Xia, F. Ma, *Mater Adv* **2022**, *3*, 624–631.

[9] Y. Li, H. Yan, B. Xu, L. Zhen, C. Y. Xu, *Adv. Mater.* **2021**, *33*, e2000581.

[10] Q. Cao, M. Kreßler, M. Hußmann, Y. Hu, P. Kusch, S. Eigler, *Chem. Mater.* **2024**, 3267–3276.

[11] a) L. Bao, B. Zhao, B. Yang, M. Halik, F. Hauke, A. Hirsch, *Adv. Mater.* **2021**, *33*, e2101653; b) L. Bao, B. Zhao, M. Assebban, M. Halik, F. Hauke, A. Hirsch, *Chem. Eur. J.* **2021**, *27*, 8709–8713.

[12] P. Vecera, S. Eigler, M. Kolesnik-Gray, V. Krstic, A. Vierck, J. Maultzsch, R. A. Schafer, F. Hauke, A. Hirsch, *Sci. Rep.* **2017**, *7*, 45165.

[13] a) L. Bao, B. Zhao, V. Lloret, M. Halik, F. Hauke, A. Hirsch, *Angew. Chem. Int. Ed.* **2020**, *59*, 6700–6705; b) R. A. Schäfer, K. Weber, M. Koleśnik-Gray, F. Hauke, V. Krstić, B. Meyer, A. Hirsch, *Angew. Chem. Int. Ed.* **2016**, *55*, 14858–14862.

[14] a) S. Mouri, Y. Miyauchi, K. Matsuda, *Nano Lett.* **2013**, *13*, 5944–5948; b) B. Chakraborty, A. Bera, D. V. S. Muthu, S. Bhowmick, U. V. Waghmare, A. K. Sood, *Phys. Rev. B* **2012**, *85*, 161403; c) H. J. Conley, B. Wang, J. I. Ziegler, R. F. Haglund Jr., S. T. Pantelides, K. I. Bolotin, *Nano Lett.* **2013**, *13*, 3626–3630.

[15] K. G. Zhou, F. Withers, Y. Cao, S. Hu, G. Yu, C. Casiraghi, *ACS Nano* **2014**, *8*, 9914–9924.

[16] a) L. Chen, H.-L. Hou, M. Prato, *Chem. Mater.* **2023**, *35*, 5032–5039; b) W. M. Parkin, A. Balan, L. Liang, P. M. Das, M. Lamparski, C. H. Naylor, J. A. Rodriguez-Manzo, A. T. Johnson, V. Meunier, M. Drndic, *ACS Nano* **2016**, *10*, 4134–4142.

[17] K. F. Mak, K. He, C. Lee, G. H. Lee, J. Hone, T. F. Heinz, J. Shan, *Nat. Mater.* **2013**, *12*, 207–211.

[18] J. P. Perdew, K. Burke, M. Ernzerhof, *Phys. Rev. Lett.* **1996**, *77*, 3865–3868.

[19] A. Tkatchenko, M. Scheffler, *Phys. Rev. Lett.* **2009**, *102*, 073005.

[20] D. Pierucci, H. Henck, J. Avila, A. Balan, C. H. Naylor, G. Patriarche, Y. J. Dappe, M. G. Silly, F. Sirotti, A. T. Johnson, M. C. Asensio, A. Ouerghi, *Nano Lett.* **2016**, *16*, 4054–4061.

[21] a) J. Quereda, A. Castellanos-Gomez, N. Agraït, G. Rubio-Bollinger, *Appl. Phys. Lett.* **2014**, *105*, 053111; b) S. Tongay, W. Fan, J. Kang, J. Park, U. Koldemir, J. Suh, D. S. Narang, K. Liu, J. Ji, J. Li, R. Sinclair, J. Wu, *Nano Lett.* **2014**, *14*, 3185–3190.

[22] a) G. Kresse, J. Furthmüller, *Phys. Rev. B* **1996**, *54*, 11169–11186; b) G. Kresse, D. Joubert, *Phys. Rev. B* **1999**, *59*, 1758–1775.

[23] P. E. Blöchl, *Phys. Rev. B* **1994**, *50*, 17953–17979.

[24] S. Singh, C. Espejo, A. H. Romero, *Phys. Rev. B* **2018**, *98*, 155309.